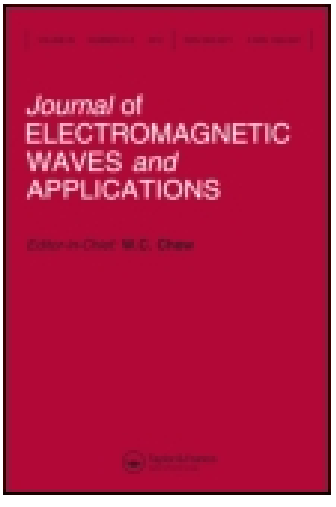

Journal of Electromagnetic Waves and Applications
Publication details, including instructions for authors and subscription information:
http://www.tandfonline.com/loi/tewa20

Forward-looking bistatic SAR imaging based on high-order range equation and high-order phase compensation

S.S. Zhang [a] & J. Li [a]
[a] Research Institute of Electronic Science and Technology , University of Electronic Science and Technology of China , Chengdu , 611731 , China
Published online: 17 Oct 2012.

To cite this article: S.S. Zhang & J. Li (2012) Forward-looking bistatic SAR imaging based on high-order range equation and high-order phase compensation, Journal of Electromagnetic Waves and Applications, 26:17-18, 2304-2314, DOI: 10.1080/09205071.2012.733499

To link to this article: http://dx.doi.org/10.1080/09205071.2012.733499

Journal of Electromagnetic Waves and Applications
Vol. 26, Nos. 17–18, December 2012, 2304–2314

Taylor & Francis
Taylor & Francis Group

Forward-looking bistatic SAR imaging based on high-order range equation and high-order phase compensation

S.S. Zhang and J. Li*

Research Institute of Electronic Science and Technology, University of Electronic Science and Technology of China, Chengdu 611731, China

(*Received 10 July 2012; accepted 7 September 2012*)

Synthetic aperture radar (SAR) techniques are typically used to achieve a high azimuth resolution, but conventional monostatic SAR is not applicable in forward direction because of azimuth ambiguities and poor Doppler resolution. This paper focuses on SAR imaging processing in a novel forward-looking bistatic configuration that a pilotless plane transmits signals and a guided missile receives echo which can avoid image ambiguities and to improve the azimuth resolution. A fourth-order range equation and a fourth-order phase term are adopted to improve the accuracy in the approximation of the range history and two-dimensional spectrum for forward-looking bistatic SAR, respectively. The spectrum is used for high-order phase compensation, range compression, secondary range compression, range cell migration correction, and azimuth compression. Especially, the proposed algorithm is able to focus the translational variant bistatic configuration where the transmitter and receiver platforms are moving in parallel tracks with different velocities and high squints. Finally, simulations validate the effectiveness of the algorithm.

1. Introduction

Synthetic aperture radar (SAR) is a radar imaging technology capable of producing high-resolution images of the stationary surface targets [1,2]. The main advantages of SAR are that it can reduce the effects of clouds and fog and allow them to be independent of external sources for imaging, having day and night and all-weather imaging capability. Bistatic SAR uses a separated transmitter and receiver moving on different platforms. This configuration is becoming prospective in the field of earth remote sensing and mapping due to its attractive features – platform flexibility, immunity to physical attacks, and electronic countermeasures [3–13].

Conventional monostatic SAR is not applicable in forward direction because of azimuth ambiguities and poor Doppler resolution. So, a monostatic forward-looking SAR demonstrator (Sector Imaging Radar for Enhanced Vision) using an array antenna was described in [14–16] from the German Aerospace Center (DLR). To improve the Doppler resolution and to avoid azimuth ambiguities without array antenna, forward-looking bistatic SAR (FL-BiSAR) configurations can be used to obtain high-resolution radar images. The FL-BiSAR uses spatially separated forward-looking receiver and side-looking transmitter. FL-BiSAR imaging continues to gain in significance due to a variety of convenient applications, such as flexibility of flight path, reduction of hardware cost, additional information, increased radar cross section, and landing assistance for aircraft in poor visibility conditions [17–19].

*Corresponding author. Email: lijing8609@hotmail.com

ISSN 0920-5071 print/ISSN 1569-3937 online

http://dx.doi.org/10.1080/09205071.2012.733499
http://www.tandfonline.com

FL-BiSAR arouses researchers' great concern, and a few investigations about the FL-BiSAR have been published. Firstly, the range history is the sum of two hyperbolic range equations, known as the double-square-root term. Therefore, the bistatic point target reference spectrum does not offer analytical simplicity of the single square root in monostatic SAR using the principle of stationary phase (PSP). Several methods of solving the spectrum have been researched, such as keystone transform [20], series reversion [21], Loffeld's bistatic formula [22], and two-dimensional (2D) principle of stationary phase [23]. In addition, FL-BiSAR systems with optimal geometry configuration have been developed [24] and several reconstruction methods and experiments ongoing [25–29].

In this paper, we present a novel FL-BiSAR configuration that a pilotless plane transmits signals and a guided missile receives echo signals, and introduce an improved FL-BiSAR imaging algorithm based on the fourth-order range equation and fourth-order phase compensation. This novel configuration plays a sufficient role in imaging the forward-looking terrain of the aerocraft, self-landing, navigation, etc. More importantly, this proposed imaging method can image the forward-looking targets with high preference and is able to focus the translational variant bistatic configuration where the transmitter and receiver platforms are moving in parallel tracks with different velocities and high squints.

The rest of this paper is organized as follows. In Section 2, the signal model of FL-BiSAR is presented. In Section 3, the image formation algorithm based on high-order range equation and high-order phase compensation is discussed in detail. The results of performance analysis and experimental results are presented in Section 4. Finally, Section 5 concludes this paper.

2. FL-BiSAR signal model

The geometry configuration of FL-BiSAR is shown in Figure 1, where the transmitter and receiver are mounted on two different platforms. The receiving antenna is forward looking, while the transmitter antenna is squint looking. θ_{SR} is the receiver's look-down angle, and θ_{ST} represents the squint angle of the transmitter. The moving velocities of transmitter and

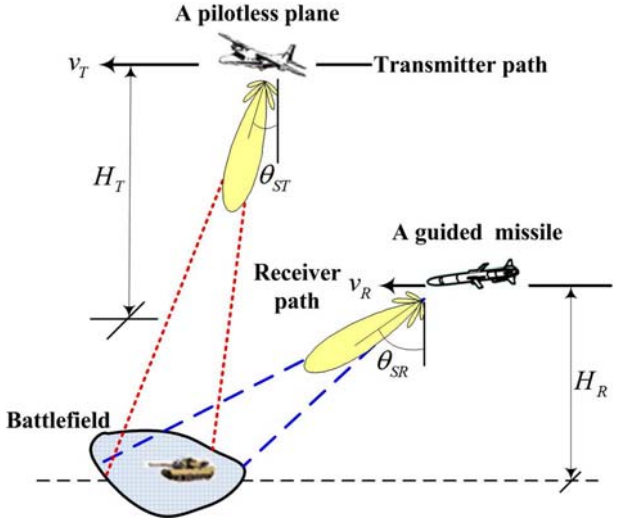

Figure 1. Geometry of FL-BiSAR.

receiver are v_T and v_R, respectively. This geometry is of advantage to guide for the missile and has been used in many civilian and military fields with its forward-looking model. $R_R(\eta)$ and $R_T(\eta)$ are the instantaneous slant ranges from the receiver and transmitter to the point target, defined as

$$R_R(\eta) = \sqrt{H_R^2 + (\eta - \eta_{R0})^2 v_R^2} \tag{1}$$

$$R_T(\eta) = \sqrt{R_{T0}^2 + (\eta - \eta_{T0})^2 v_T^2} \tag{2}$$

where η is the slow time. η_{T0} and η_{R0} are the instantaneous slow time of the transmitter and receiver to the sensor position at $\eta = 0$, respectively. R_{T0} is the transmitted range to the sensor position at $\eta = 0$, and H_R represents the receiver plat height.

Suppose the transmitted signal is linear frequency modulated signal. After mixing down and quadrature demodulation to baseband, the received radar signal is given by

$$s_R(t, \eta) = \text{rect}\left(\frac{t - R(\eta)/c}{T_p}\right) \times \exp\left\{j\pi k_r \left(t - \frac{R(\eta)}{c}\right)^2 - j\frac{2\pi R(\eta)}{\lambda}\right\} \tag{3}$$

where $R(\eta) = R_T(\eta) + R_R(\eta)$. t is the fast time, c is the speed of light, λ is the wavelength of the transmitted signal, T_p is the pulse duration, k_r is the chirp rate, and rect$(\cdot)$ is the stand for the unit rectangular function.

3. Imaging formation algorithm

3.1. 2D spectrum of FL-BiSAR

A fourth-order range equation deduced by means of vector analysis can be expressed as [21]

$$R(\eta) = R_T(\eta) + R_R(\eta) \approx k_0 + k_1\eta + k_2\eta^2 + k_3\eta^3 + k_4\eta^4 \tag{4}$$

We can get the coefficients via Taylor series. The coefficients are given by

$$k_0 = R_{T0}\sec\theta_{ST} + R_{R0}\sec\theta_{SR} \tag{5}$$

$$k_1 = v_T\sin\theta_{ST} + v_R\sin\theta_{SR} \tag{6}$$

$$k_2 = \frac{v_T^2}{2}\frac{\cos^3\theta_{ST}}{R_{T0}} + \frac{v_R^2}{2}\frac{\cos^3\theta_{SR}}{H_R} \tag{7}$$

$$k_3 = -\frac{v_T^3}{2}\frac{\cos^4\theta_{ST}\sin\theta_{ST}}{R_{T0}^2} - \frac{v_R^3}{2}\frac{\cos^4\theta_{SR}\sin\theta_{SR}}{H_R^2} \tag{8}$$

$$k_4 = \frac{v_T^4}{8}\frac{\cos^7\theta_T(4\tan^2\theta_T - 1)}{R_{T0}^3} + \frac{v_R^4}{8}\frac{\cos^7\theta_R(4\tan^2\theta_R - 1)}{H_R^3} \tag{9}$$

It is difficult to derive the FL-BiSAR point target reference 2D spectrum using the PSP as monostatic SAR because the range history is the sum of two hyperbolic range equations, known as double-square-root term. Fortunately, the method of series reversion [21] (Appendix A) is introduced to derive the 2D spectrum of echo data of the FL-BiSAR and repeated here for convenience as

$$S(f_t,f_\eta) = W_r(f_t)W_{az}\left(f_a + \frac{(f_c+f_r)k_1}{c}\right)\exp\{j\Phi(f_t,f_\eta)\} \tag{10}$$

where $W_r(\cdot)$ represents the spectral shape of the transmitted pulse and $W_{az}(\cdot)$ represents the shape of the Doppler spectrum. The phase function is given by

$$\begin{aligned}\Phi(f_t,f_\eta) = &-\frac{\pi f_t^2}{k_r} - \frac{2\pi(f_c+f_t)}{c}k_0 + \frac{\pi}{2k_2}\left(\frac{c}{f_c+f_t}\right)\\ &\times\left(f_\eta + \frac{(f_c+f_t)k_1}{c}\right)^2 + \frac{\pi k_3}{4k_2^3}\left(\frac{c}{f_c+f_t}\right)^2\left(f_\eta + \frac{(f_c+f_t)k_1}{c}\right)^3 + \left(\frac{9k_3^2-4k_4k_2}{32k_2^5}\right)\pi\left(\frac{c}{f_c+f_t}\right)^3\left(f_\eta + \frac{(f_c+f_r)k_1}{c}\right)^4\end{aligned} \tag{11}$$

where f_t is the range frequency, f_η is the azimuth frequency, and f_c is the carrier frequency. To facilitate the development of processing algorithms, (11) is expanded in a power series of f_t, and the terms are kept up to the fourth-order:

$$\Phi(f_t,f_\eta) \approx \Phi(0,f_\eta) + \Phi'(0,f_\eta)f_t + \frac{1}{2}\Phi''(0,f_\eta)f_t^2 + \frac{1}{6}\Phi'''(0,f_\eta)f_t^3 + \frac{1}{24}\Phi''''(0,f_\eta)f_t^4 \tag{12}$$

3.2. *Imaging processing*

We can decompose $\Phi(f_t, f_\eta)$ into range compression term, azimuth compression term, secondary range compression (SRC) term, range cell migration (RCM) term, the third-order term, and the fourth-order term, denoted by the subscripts rc, ac, src, rcm, $3rd$, and $4th$, respectively. Thus, the phase function shown in (12) can be further rewritten as

$$\Phi(f_t,f_\eta) \approx \phi_{rc}(f_t) + \phi_{src}(f_t,f_\eta) + \phi_{rcm}(f_t,f_\eta) + \phi_{ac}(f_\eta) + \phi_{3rd}(f_t,f_\eta) + \phi_{4th}(f_t,f_\eta) \tag{13}$$

Each of these phase terms can be interpreted as follows:

- The first phase term $\phi_{rc}(f_t)$ is quadratic in the range frequency variable and thus responsible for the range modulation as

$$\phi_{rc}(f_t) = -\frac{\pi f_t^2}{k_r} \tag{14}$$

This phase term is dependent only on f_t and thus can be separated from the other phase terms. Range compression uses a phase multiply to remove this phase term.

- The second phase term $\phi_{src}(f_t, f_\eta)$ represents SRC term. This phase term is the remaining contribution that depends on f_t and f_η. It is very important for accurate focusing when the squint is high and the wavelength long. It can be expressed as

$$\begin{aligned}\phi_{src}(f_t,f_\eta) = &\frac{\pi k_1^2 f_t^2}{2k_2 c f_c} + \frac{3\pi k_3 k_1^2 - 4\pi k_1 k_2^2}{4k_2^3 f_c^2} f_t^2 \left(f_\eta + \frac{f_c k_1}{c}\right) \\ &+ \frac{8k_2^4 + 27k_3^2 k_1^2 - 12k_4 k_2 k_1^2 - 24k_3 k_2^2 k_1}{16k_2^5 f_c^3} f_t^2 c\pi \left(f_\eta + \frac{f_c k_1}{c}\right)^2 \\ &+ \frac{-27k_3^2 k_1 + 12k_4 k_2 k_1 + 6k_3 k_2^2}{8k_2^5 f_c^4} f_t^2 c^2 \pi \left(f_\eta + \frac{f_c k_1}{c}\right)^3 + \frac{27k_3^2 - 12k_4 k_2}{16k_2^5 f_c^5} f_t^2 c^3 \pi \left(f_\eta + \frac{f_0 k_1}{c}\right)^4\end{aligned} \tag{15}$$

- The third phase term $\phi_{rcm}(f_t, f_\eta)$ represents the range cell migration term as

$$\begin{aligned}\phi_{rcm}(f_t,f_\eta) = &-\frac{2\pi f_t}{c} k_0 + \frac{\pi k_1 f_t}{k_2 f_c}\left(f_\eta + \frac{f_c k_1}{c}\right) + \frac{\pi c f_t (3k_3 k_1 - 2k_2^2)}{4k_2^3 f_c^2}\left(f_\eta + \frac{f_c k_1}{c}\right)^2 \\ &+ \frac{c^2 \pi f_t (9k_3^2 k_1 - 4k_2^2 k_3 - 4k_4 k_2 k_1)}{8k_2^5 f_c^3}\left(f_\eta + \frac{f_c k_1}{c}\right)^3 + \frac{-27k_3^2 + 12k_4 k_2}{32k_2^5 f_c^4} c^3 \pi f_t \left(f_\eta + \frac{f_c k_1}{c}\right)^4\end{aligned} \tag{16}$$

This term represents the range variant feature of the derived spectrum within the scene. After RCM correction (RCMC), most of the energy from the point target falls into one range cell.

- The fourth phase term $\phi_{ac}(f_\eta)$ represents the azimuth modulation. It is solely dependent on f_η and will be removed by the azimuth-matched filtering after RCM correction in the range-Doppler domain.

$$\phi_{ac}(f_\eta) = -\frac{2\pi k_0 f_c}{c} + \frac{\pi c}{2k_2 f_c}\left(f_\eta + \frac{f_c k_1}{c}\right)^2 + \frac{\pi c^2 k_3}{4f_c^2 k_2^3}\left(f_\eta + \frac{f_c k_1}{c}\right)^3 + \left(\frac{9k_3^2 - 4k_4 k_2}{32k_2^5}\right)\frac{\pi c^3}{f_c^3}\left(f_\eta + \frac{f_\eta k_1}{c}\right)^4 \tag{17}$$

- The fifth and sixth terms of (13) are the residual phase term. $\phi_{3rd}(f_t, f_\eta)$ and $\phi_{4th}(f_t, f_\eta)$ represent the third-order phase term and fourth phase term. It is independent of the range and azimuth frequency variables and can be ignored if a magnitude image is the final product. If the phase information is required, these residual terms need to be compensated in the image domain by using a phase multiplication. In this paper, we propose a novel FL-BiSAR configuration with high squint and translational variant case. Thereby, its effect of high residual phase terms cannot be neglected and must be considered in the FL-BiSAR cases. The expressions of the third and fourth terms are

$$\phi_{3rd}(f_t,f_\eta) = -\frac{\pi k_1^2 f_t^3}{2k_2 f_c^2 c} + \frac{\pi k_3 k_1^3 f_t^3}{4k_2^3 f_c^2 c} + \frac{8k_2^4\pi k_1 - 12\pi k_3 k_1^2 k_2^2 + (9k_3^2 - 4k_4k_2)\pi k_1^3}{8k_2^5 f_c^3} f_t^3 \left(f_\eta + \frac{f_c k_1}{c}\right) + \frac{36\pi k_2^2 k_3 k_1 c - 8\pi k_2^4 c - 9(9k_3^2 - 4k_4k_2)\pi c k_1^2}{16k_2^5 f_c^4} f_t^3 \left(f_\eta + \frac{f_c k_1}{c}\right)^2 + \frac{3(9k_3^2 - 4k_4k_2)\pi c^2 k_1 - 4\pi k_2^2 k_3 c_2^2}{4k_2^5 f_c^5} f_t^3 \left(f_\eta + \frac{f_c k_1}{c}\right)^3 - \frac{5(9k_3^2 - 4k_4k_2)\pi c^3 f_t^3}{16k_2^5 f_c^6} \left(f_\eta + \frac{f_c k_1}{c}\right)^4 \quad (18)$$

$$\phi_{4th}(f_t,f_\eta) = \frac{\pi k_1^2 f_t^4}{2k_2 f_c^3 c} - \frac{\pi k_3 k_1^3 f_t^4}{2k_2^3 f_c^3 c} + \frac{(9k_3^2 - 4k_4k_2)\pi k_1^4 f_t^4}{32k_2^5 f_c^3 c} + \frac{18\pi k_3 k_1^2 k_2^2 - 8\pi k_1 k_2^4 - 3(9k_3^2 - 4k_4k_2)\pi k_1^3}{8k_2^5 f_c^4} f_t^4 \left(f_\eta + \frac{f_c k_1}{c}\right) + \frac{4\pi c k_2^4 - 24\pi c k_3 k_1 k_2^2 + 9\pi c(9k_3^2 - 4k_4k_2)k_1^2}{8k_2^5 f_c^5} f_t^4 \left(f_\eta + \frac{f_c k_1}{c}\right)^2 + \frac{5\pi c^2 k_3 k_2^2 - 5(9k_3^2 - 4k_4k_2)\pi c^2 k_1}{4k_2^5 f_c^6} f_t^4 \left(f_\eta + \frac{f_c k_1}{c}\right)^3 + \frac{15(9k_3^2 - 4k_4k_2)\pi c^3}{32k_2^5 f_c^7} f_t^4 \left(f_\eta + \frac{f_c k_1}{c}\right)^4 \quad (19)$$

Based on the aforementioned description, the processing steps of the proposed approach are shown in Figure 2, where Fourier transform and inverse Fourier transform represent, FT and IFT respectively.

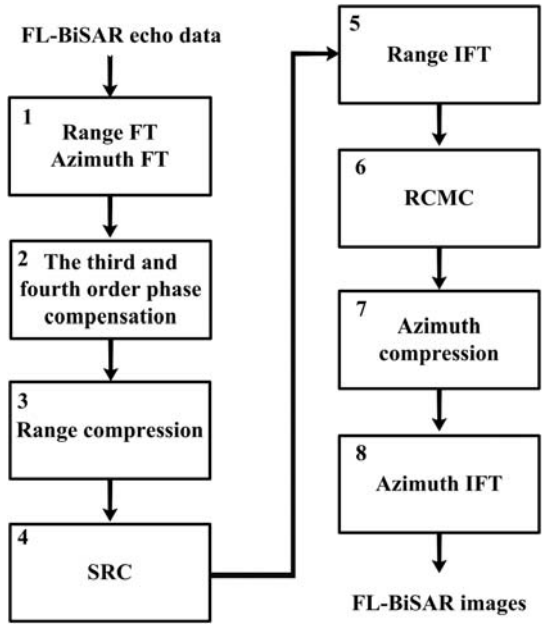

Figure 2. Block diagram of RDA for FL-BiSAR.

3.3. Phase error limits

The accuracy of the spectrum is limited by the number of terms used in the expansion of (12). In general, we would like to limit the uncompensated phase error ϕ_E within $\pm\frac{\pi}{4}$, in order to avoid significant deterioration of image quality. So, a phase error of $\pm\frac{\pi}{4}$ is usually used as an upper limit to obtain a good focusing quality,

$$|\phi_E| \leq \frac{\pi}{4} \tag{20}$$

4. Simulation results

4.1. Point scatterers simulation

To prove the validity of the formulation, five point targets' signals are simulated in the scene as shown in Figure 3(a), where point O is located in the center of the scene, and the other four targets are located on the vertices of a 500 m. The relative coordinates are listed as follows (m, m) : $O(0, 0)$, $A(-20, -20)$, $B(20, -20)$, $C(-20, 20)$, and $D(20, 20)$. The simulation radar parameters are listed in Table 1.

Processing efficiency is achieved by focusing point targets in an invariance region with the same matched filter. The simulated compression results of the five point targets are shown

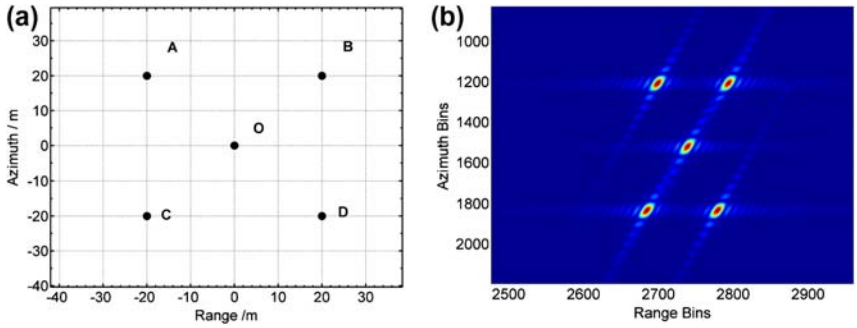

Figure 3. Imaging results with point targets. (a) Simulated scene with three point targets. (b) Point targets focused using the FL-BiSAR RDA.

Table 1. Simulated radar parameters.

Simulation parameters	Transmitter	Receiver
Velocity in x direction	0 m/s	0 m/s
Velocity in y direction	200 m/s	300 m/s
Velocity in z direction	0 m/s	0 m/s
Carrier frequency	35 GHz	
PRF	1000 Hz	
Central range	52 km	
Pulse duration	12.5 μs	
Transmitted signal bandwidth	300 MHz	
Platform height	8 km	6 km
Squint angle	0°	60°

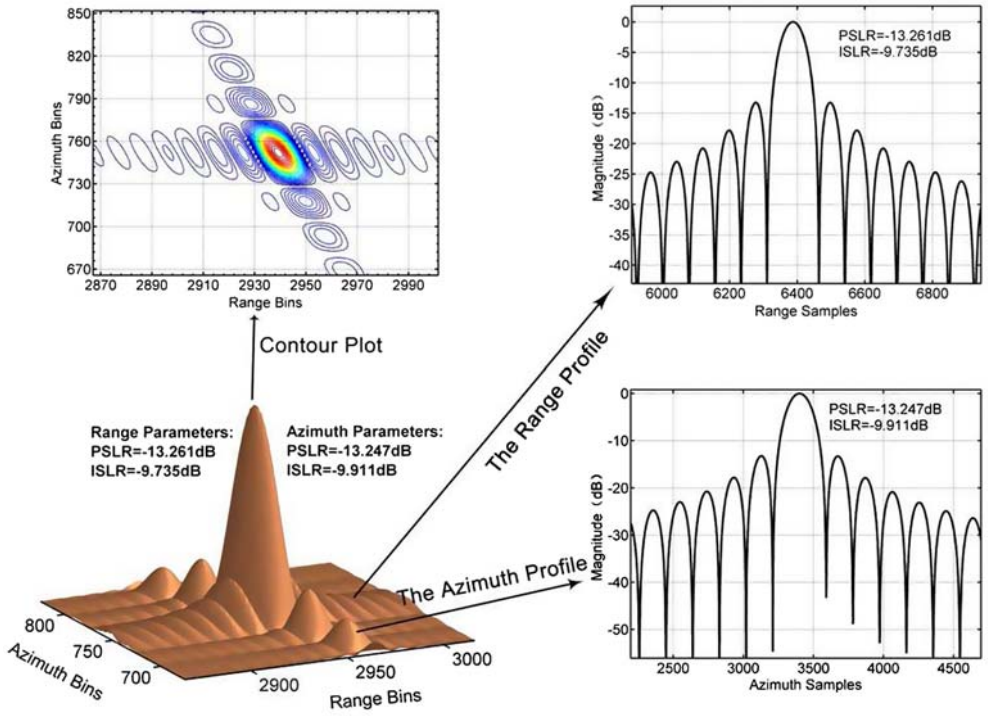

Figure 4. Measurement of point target focus for point target *O*.

in Figure 3(b). The results demonstrate that the proposed algorithm can give accurate focusing in the FL-BiSAR configuration.

Furthermore, a point target located at the central scene is used for measurement. To quantify the precision of the presented processing method, the peak side lobe ratio (PSLR) and integrated side lobe ratio (ISLR) are used as quality criteria. And, the measurement of point target focus for point target *O* is shown as Figure 4. The left figures are two-dimensional impulse response and contour plot. The right figures are the range profile and azimuth profile. The point target quality measurements for other targets are given in Table 2.

4.2. *The influence of the high expansion order and spectrum error*

To visually contrast the influence of the high-order phase factor, we simulate the point target imaging with and without high-order phase compensation, respectively. The results are shown in

Table 2. Point target imaging performance.

		PSLR (dB)	ISLR (dB)
Point *A*	Range	−13.2569	−9.7922
	Azimuth	−13.2512	−10.0539
Point *B*	Range	−13.2581	−9.7923
	Azimuth	−13.2083	−10.0063
Point *C*	Range	−13.2624	−9.7917
	Azimuth	−13.1771	−9.9271
Point *D*	Range	−13.2619	−9.7920
	Azimuth	−13.2342	−9.9899

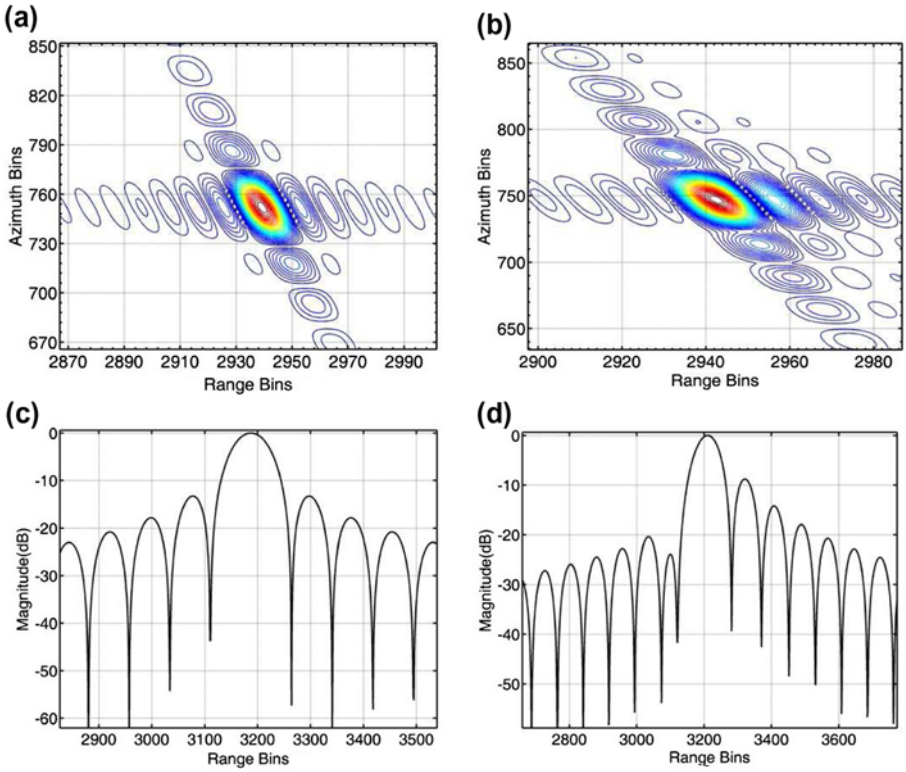

Figure 5. The influence of the high expansion order. (a) Imaging with high-order phase compensation. (b) Imaging without high-order phase compensation. (c) Range profile with high-order phase compensation. (d) Range profile without high-order phase compensation.

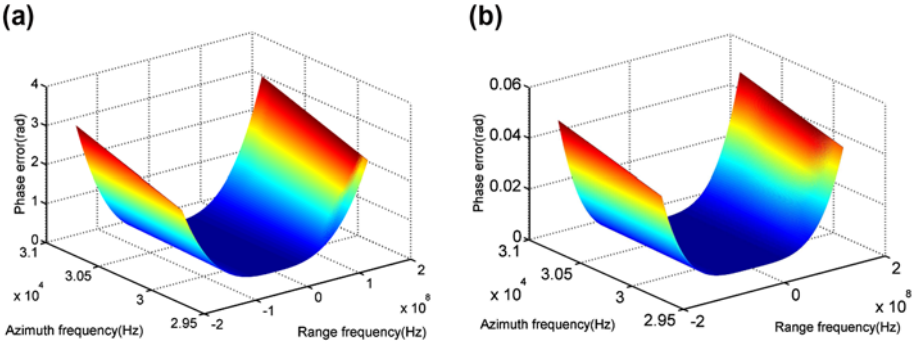

Figure 6. Spectrum phase errors in the FL-BiSAR configurations. (a) The third-order phase error in terms of 2D frequency. (b) The fourth-order phase error in terms of 2D frequency.

Figure 5. With the same scene and parameters, we find that the imaging performance with high-order phase compensation is better than the method without high-order phase compensation.

Figure 6(a) and (b) are the third and fourth phase errors in FL-BiSAR configurations, respectively. The phase component $|\Delta\phi_{3\mathrm{rd}}|$ is more than $\frac{\pi}{4}$ and $|\Delta\phi_{4\mathrm{th}}|$ much less than $\frac{\pi}{4}$.

Therefore, it is sufficient to retain only terms up to the quartic term in the phase expansion (12) for accurate focusing in this FL-BiSAR case.

From Figures 5 and 6, we can find that the high-order phase compensation is required in FL-BiSAR imaging.

5. Conclusion

In this paper, we present a novel FL-BiSAR configuration that a pilotless plane transmits signals with squint looking and a guided missile receives echo signals with forward looking. The phase error analysis shows that the third-order phase term cannot be ignored in FL-BiSAR. Thus, we propose a FL-BiSAR RD imaging algorithm based on the fourth-order range equation and fourth-order phase compensation. The simulation results and analysis validate the effectiveness of the proposed method in this FL-BiSAR configuration.

Acknowledgement

This work was supported by the Fundamental Research Funds for the Central Universities of China under No. ZYGX2010J118.

References

[1] Chan YK, Koo VC. An introduction to synthetic aperture radar (SAR). Prog. Electromagnet. Res. B. 2008;2:27–60.
[2] Chan YK, Lim SY. Synthetic aperture radar (SAR) signal generation. Prog. Electromagnet. Res. B. 2008;1:269–290.
[3] Kassem MJB, Saillard J, Khenchaf A. BISAR mapping I. Theory and modeling. Prog. Electromagnet. Res. 2006;61:39–65.
[4] Kassem MJB, Saillard J, Khenchaf A. BISAR mapping II. Treatment, simulation and experimentation. Prog. Electromagnet. Res. 2006;61:67–87.
[5] Krieger G, Moreira A. Spaceborne bi- and multistatic SAR: potentials and challenges. IEE Proc. Radar Sonar Navig. 2006;153:184–198.
[6] Ender JHG. A step to bistatic SAR processing. In: European Conference on Synthetic Aperture Radar (EUSAR '04); 2004 May; Ulm, Germany. p. 356–359.
[7] Wu J, Yang J, Huang Y, Liu Z, Yang H. A new look at the point target reference spectrum for bistatic SAR. Prog. Electromagnet. Res. 2011;119:363–379.
[8] Sun J, Mao S, Wang G, Hong W. Polar format algorithm for spotlight bistatic SAR with arbitrary geometry configuration. Prog. Electromagnet. Res. 2010;103:323–338.
[9] Zhao YW, Zhang M, Geng XP, Zhou P. A comprehensive facet model for bistatic SAR imagery of dynamic ocean scene. Prog. Electromagnet. Res. 2012;123:427–445.
[10] Sun J, Mao S, Wang G, Hong W. Extended exact transfer function algorithm for bistatic SAR of translational invariant case. Prog. Electromagnet. Res. 2009;99:89–108.
[11] Ji W-J, Tong C-M. Bistatic scattering from two-dimensional dielectric ocean rough surface with a PEC object partially embedded by using the G-SMCG method. Prog. Electromagnet. Res. 2010;105:119–139.
[12] Liu Q, Hong W, Tan W, Lin Y, Wang Y, Wu Y. An improved polar format algorithm with performance analysis for geosynchronous circular SAR 2D imaging. Prog. Electromagnet. Res. 2011;119:155–170.
[13] Guo D, Xu H, Li J. Extended wavenumber domain algorithm for highly squinted sliding spotlight SAR data processing. Prog. Electromagnet. Res. 2011;114:17–32.
[14] Sutor T, Witte F, Moreira A. A new sector imaging radar for enhanced vision: SIREV. Proc. SPIE. 1999 Jan;3691:39–47.
[15] Krieger G, Mittermayer J, Wendler M, Witte F, Moreira A. SIREV – Sector imaging radar for enhanced vision. Proceedings of the 2nd International Symposium on Image and Signal Processing and Analysis, ISPA 2001; 2001 Jun. p. 377–382. doi: 10.1109/ISPA.2001.938659.
[16] Krieger G, Mittermayer J, Wendler M, Witte F, Moreira A. SIREV – Sector imaging radar for enhanced vision. Aerosp. Sci. Technol. 2003 Mar;7:147–158.

[17] Pinel N, Bourlier C, Saillard J. Forward radar propagation over oil slicks on sea surfaces using the ament model with shadowing effect. Prog. Electromagnet. Res. 2007;76:95–126.
[18] Qu Y, Liao G, Zhu S-Q, Liu X-Y. Pattern synthesis of planar antenna array via convex optimization for airborne forward looking radar. Prog. Electromagnet. Res. 2008;84:1–10.
[19] Balke J. Bistatic forward-looking synthetic aperture radar. Proceedings of RADAR; 2004 Oct; Toulouse, France.
[20] Dai CY, Zhang XL. Bistatic SAR image formation algorithm using keystone transform. In: 2011 IEEE Radar Conference (RADAR). 2011 May. p. 342–345. doi: 10.1109/RADAR.2011.5960556.
[21] Neo YL, Wong F, Cumming I. A two-dimensional spectrum for bistatic SAR processing using series reversion. IEEE Geosci. Remote Sens. Lett. Jan. 2007;4:93–96.
[22] Loffeld O, Nies H, Peters V, Knedlik S. Models and useful relations for bistatic SAR processing. IEEE Trans. Geosci. Remote Sens. 2004 Oct.; 42:2031–2038.
[23] Wang R, Deng YK, Loffeld O, Nies H, Walterscheid I, Espeter T, Klare J, Ende JHG. Processing the azimuth-variant bistatic SAR data by using monostatic imaging algorithms based on two-dimensional principle of stationary phase. IEEE Trans. Geosci. Remote Sens. 2011 Apr;49:3504–3520.
[24] Wu JJ, Yang JY, Yang HG, Huang YL. Optimal geometry configuration of bistatic forward-looking SAR. In: IEEE International Conference on Acoustics, Speech and Signal Processing, ICASSP 2009; 2009 Apr. p. 1117–1120. doi: 10.1109/ICASSP.2009.4959784.
[25] Li WC, Huang YL, Yang JY, Wu JJ, Kong LJ. An improved Radon-transform-based scheme of doppler centroid estimation for bistatic forward-looking SAR. IEEE Geosci. Remote Sens. Lett. 2011 Mar;8:379–383.
[26] Shin HS, Lim JT. Omega-k algorithm for airborne forward-looking bistatic spotlight SAR imaging. IEEE Geosci. Remote Sens. Lett. 2009 Apr;6:312–316.
[27] Thomas E, Walterscheid I, Klare J, Brenner AR, Ender HG. Bistatic forward-looking SAR: results of a spaceborne-airborne experiment. IEEE Geosci. Remote Sens. Lett. 2011 Jul;8:765–768.
[28] Qiu X, Hu D, Ding C. Some reflections on bistatic SAR of forward-looking configuration. IEEE Geosci. Remote Sens. Lett. 2008 Oct;5:735–739.
[29] Ren XZ, Sun JT, Yang RL. A new three-dimensional imaging algorithm for airborne forward-looking SAR. IEEE Geosci. Remote Sens. Lett. 2011 Jan;8:153–157.

Appendix A

Series reversion [21] is used get the coefficients of (A1) via its inverse function. For a function expressed in a series with no constant term,

$$y = a_1 x + a_2 x^2 + a_3 x^3 + \dots. \tag{A1}$$

The series expansion of the inverse function is given by

$$x = A_1 y + A_2 y^2 + A_3 y^3 + \dots. \tag{A2}$$

Substituting (A2) into (A1), we can get the equation:

$$y = a_1 A_1 y + (a_2 A_1^2 + a_1 A_2) y^2 + (a_3 A_1^3 + 2a_1 A_1 A_2 + a_1 A_3) y^3 + \dots. \tag{A3}$$

Contrasting Equations (A1) and (A3), the coefficients are obtained as follows:

$$\begin{aligned} A_1 &= a_1^{-1} \\ A_2 &= -a_1^{-3} a_2 \\ A_3 &= a_1^{-5}(2a_2^2 - a_1 a_3) \\ &\dots \end{aligned} \tag{A4}$$